View metadata, citation and similar papers at core.ac.uk

brought to you by CORE

provided by Cork Open Research Archive

Title	Optical response of nanostructured surfaces: experimental investigation of the composite diffracted evanescent wave model
Author(s)	Gay, G.; Alloschery, O.; De Viaris Lesegno, B.; O'Dwyer, Colm; Lezec, H. J.
Publication date	2006-02
Original citation	Gay, G., Alloschery, O., Lesegno, B. V. d., O'Dwyer, C., Lezec, H. and Weiner, J. (2006) 'Optical response of nanostructured surfaces: experimental investigation of the composite diffracted evanescent wave model', SPIE Proceedings Volume 6131, Nanomanipulation with Light II; 61310J, 09 February. doi: 10.1117/12.640924
Type of publication	Article (peer-reviewed)
Link to publisher's version	https://doi.org/10.1117/12.640924 http://dx.doi.org/10.1117/12.640924 Access to the full text of the published version may require a subscription.
Rights	**© (2006) COPYRIGHT Society of Photo-Optical Instrumentation Engineers (SPIE).**
Item downloaded from	http://hdl.handle.net/10468/6298

Downloaded on 2018-06-19T07:54:22Z

Optical Response of Nanostructured Surfaces: Experimental Investigation of the Composite Diffracted Evanescent Wave Model

G. Gay[a], O. Alloschery[a], B. Viaris de Lesegno[b], C. O'Dwyer[c], H. Lezec[d] and J. Weiner[a]

[a] IRSAMC/LCAR, Université Paul Sabatier, 118 route de Narbonne, 31062 Toulouse, France
[b] Laboratoire Aimé Cotton, Campus d'Orsay, 91405 Orsay, France
[c] Photonic Nanostructures Group Tyndall National Institute, Lee Maltings, Cork, Ireland
[d] T. J. Watson Laboratories of Applied Physics, California Institute of Technology, Pasadena, California 91125 USA

ABSTRACT

The past decade has seen a rapidly developing interest in the response of subwavelength-structured surfaces to optical excitation. Many studies have interpreted the optical coupling to the surface in terms of surface plasmon polaritons, but recently another approach involving diffraction of surface evanescent waves, the Composite Diffractive Evanescent Wave (CDEW) model has been proposed. We present here a series of measurements on very simple one-dimensional (1-D) subwavelength structures with the aim of testing key properties of the surface waves predicted by the CDEW model.

Keywords: surface waves, surface plasmons, diffraction, subwavelength, enhanced transmission

1. INTRODUCTION

Initial reports of dramatically enhanced transmission through arrays of subwavelength holes in thin films and membranes [1–3] have focused attention on the physics underlying this surprising optical response. Since the early experiments were carried out on metal films, surface plasmon polaritons [4,5] were invoked to explain the anomalously high transmission and to suggest new types of photonic devices.[5] Other interpretations based on "dynamical diffraction" in periodic slit and hole arrays [6,7] or various kinds of resonant cavity modes in 1-D slits and slit arrays [8,9] have also been proposed. Reassessment of the earlier data and new measurements have prompted a sharp downward revision of the enhanced transmission factor from $\simeq 1000$ to $\simeq 10$ and have motivated the development of a new model of surface wave excitation termed the composite diffracted evanescent wave (CDEW) model.[10] This model builds a composite surface wave from the large distribution of evanescent modes (the inhomogeneous modes of the "angular spectrum representation" of wave fields [11]) launched by a subwavelength feature such as a hole, slit, or groove when subjected to an external source of propagating plane wave excitation. The CDEW model predicts three specific surface wave properties. First, the surface wave is a composite or "wave packet" of modes evanescent in the initial source propagation direction with well-defined nodal positions spaced by a characteristic wavelength, λ_{cd}; second, the appearance of the first node at a distance of $\lambda_{\mathrm{cd}}/2$ from the subwavelength launch site; and third, an amplitude decreasing inversely with distance from the launch site. We present here the results of a series of experiments on very simple 1-D subwavelength surface structures designed to investigate these predictions and thus assess the validity of the model.

2. SUMMARY OF THE CDEW MODEL

The essential elements of the CDEW model can best be summarised with reference to Fig. 1. It is based on a solution to the 2-D Helmholtz equation in the near field and subject to the slab-like boundary conditions of a slit in an opaque screen. The basic expression describing the scalar wave is

$$\left[\nabla^2 + k^2\right] E(x,z) = 0 \tag{1}$$

Send correspondence to jweiner@irsamc.ups-tlse.fr

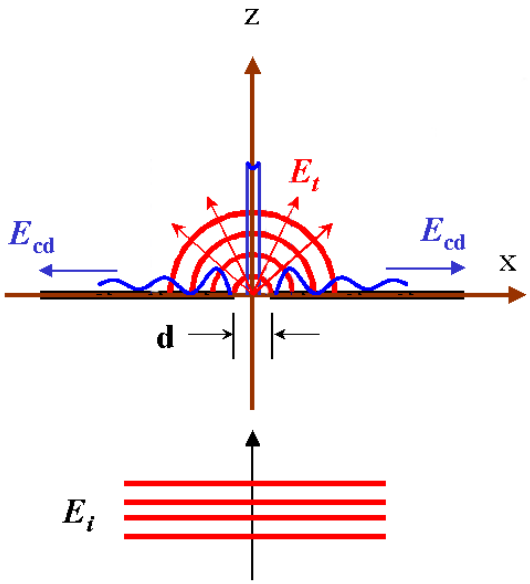

Figure 1. Schematic diagramme of the CDEW model: A plane wave E_i with $k_0 = 2\pi/\lambda_0$, incoming from below, impinges on a subwavelength slit of width d. A fraction of the incoming light is directly transmitted E_t and indicated by the red cylindrical wave fronts emanating from the centre of the slit into the positive z half-space. Another fraction of the incoming light $E_{\rm cd}$ (blue trace) is launched along the surface in the $\pm x$ directions as the composite evanescent wave.

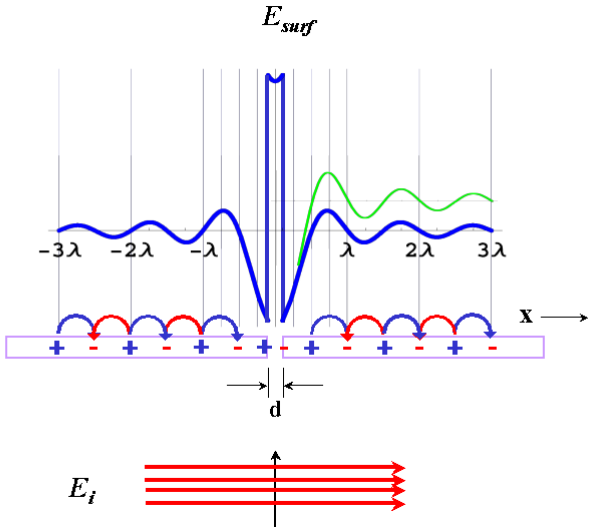

Figure 2. Detail of the CDEW shown in Fig. 1. The incoming plane wave is linearly polarised parallel to the plane of the structure and perpendicular to the slit. The alternating blue and red loops indicate the field lines induced by the CDEW near the surface of the silver film. The blue trace above the structure presents a more detailed view of the $E_{\rm cd}$ shown in Fig. 1 and calculated from Eqs. 2a, 2b. The green trace above $E_{\rm cd}$ shows the cosine representation of $E_{\rm cd}$ expressed by Eq. 4 and closely approximating Eq. 2a for $|x| \geq 3/4\,\lambda$.

with $\nabla^2 = \partial^2/\partial x^2 + \partial^2/\partial z^2$, $k = 2\pi/\lambda$ and $E(x,z)$ the amplitude of the wave propagating in the x, z directions. Kowarz [12] has written down the solution to this equation for the case of an incident plane wave with amplitude E_0 and propagation vector k_0 impinging on a slit of width d in an opaque screen. Specifying the coordinates as shown in Fig. 1, the field solution E_{ev} for the modes evanescent in z at the $z = 0$ boundary is

$$E_{ev}(x, z=0) = -\frac{E_0}{\pi}\left\{\mathrm{Si}\left[k\left(x+\frac{d}{2}\right)\right] - \mathrm{Si}\left[k\left(x-\frac{d}{2}\right)\right]\right\} \quad \text{for} \quad |x| > d/2 \tag{2a}$$

$$= \frac{E_0}{\pi}\left\{\pi - \mathrm{Si}\left[k\left(x+\frac{d}{2}\right)\right] + \mathrm{Si}\left[k\left(x-\frac{d}{2}\right)\right]\right\} \text{ for } |x| \leq d/2; \quad \mathrm{Si}(\alpha) \equiv \int_0^\alpha \frac{\sin(t)}{t} dt \tag{2b}$$

The k_z evanescent modes are defined by a conservation-of-energy criterion,

$$k_z = \sqrt{k_0^2 - k_x^2} \qquad k_x > k_0 \tag{3}$$

The form of the inhomogeneous or evanescent field on the $z = 0$ boundary is shown in Fig. 1 and in greater detail in Fig. 2 (blue curves in each figure). At transverse displacements from the slit $|x| > d/2$, the evanescent component of the field at the surface $E_{ev}(x, z = 0)$ can be represented to good approximation by the expression

$$E_{ev} \simeq \frac{E_0}{\pi}\frac{d}{x}\cos\left(k_{\rm cd}x + \pi/2\right) \tag{4}$$

that describes a damped harmonic wave with amplitude decreasing as the inverse of the distance from the launching edge of the slit and a phase shift of $\pi/2$ with respect to the propagating plane wave at the midpoint of the slit. This surface wave is actually a composite superposition of k_x modes evanescent in z, with $|k_x| > k_0$

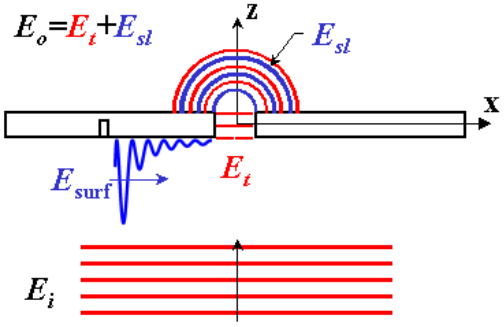

Figure 3. The incoming plane wave E_i impinges on the subwavelength slit (or hole) and a groove milled on the input side. The evanescent $E_{\rm cd}$ wave, launched on the surface at the position of the groove x_{sg} (see Fig. 4), is indicated in blue. In the model proposed in [10] CDEWs travel along the surface toward the slit where they reconvert to a propagating field E_{sl} and interfere with E_t, the propagating field directly transmitted through the slit. The superposed output field $E_o = E_t + E_{sl}$ propagates into the $z \geq 0$ half-space and the intensity of the interference figure $I(\theta)$ is detected in the far field.

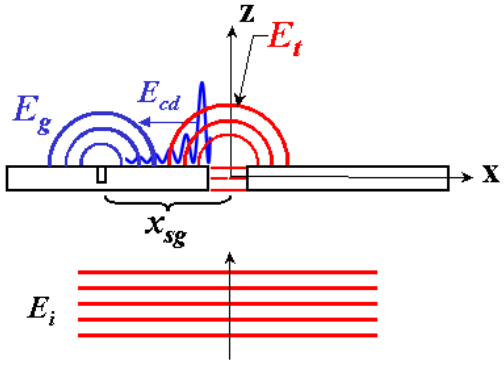

Figure 4. The incoming plane wave E_i propagates through the slit and launches surface waves along $\pm x$ on the output-side surface. The composite wave $E_{\rm cd}$, evanescent in z and indicated in blue, travel away from the slit until it encounters a groove where it is reconverted to propagating modes E_g that interferes with the propagating mode directly transmitted through the slit E_t. The interference pattern is detected in the far-field by a photodetector in the $z \geq 0$ half-space.

and directed along the $\pm x$ axes.

$$E_{ev}(x,z) = \frac{E_0}{\pi} \int_{\pm k_0}^{\pm\infty} dk_x \frac{\sin(k_x\, d/2)}{k_x} \exp(ik_x\, x) \exp(-k_z z) \tag{5}$$

Equation 5 generalises the expressions of Eqs. 2a, 2b to include the evanescent components above the surface. When the composite evanescent wave encounters a surface discontinuity (groove or hole), a fraction of the intensity is reconverted to a distribution of "homogeneous" or propagating modes $|\mathbf{k}| = 2\pi/\lambda_0|$ at the site of the groove or hole. In a practical experiment, any real planar structure has two surfaces: an "input side" in the half-space $z < 0$, containing the incoming plane wave, and an "output side" in the half-space $z \geq 0$, containing the far-field propagating modes issuing from the output surface and a photodetector. As shown in the diagrammes of Figs. 3, 4 experiments can be carried out by fabricating subwavelength grooves on the input, the output side or both.

3. EXPERIMENTAL

3.1. Structure fabrication

The subwavelength structures are fabricated by focused ion beam (FIB) milling (FEI Nova-600 Dual-Beam system, Ga^+ ions, 30keV)in a 400 nm thick layer of silver evaporated onto flat fused silica microscope slides. A low beam current (50 pA) was used in order to achieve surface features defined with a lateral precision on the order of 10 nm and characterised by near-vertical sidewalls and a minimal amount of edge rounding. Since it enables delivery of a variable ion dose to each pixel of the writing field, FIB milling conveniently allows the multiple-depth topography characteristic of the present devices to be formed in a single, self-aligned step. A 2-D matrix of structures is milled into the silver layer. Each matrix consists of 63 structures, nine columns, separated by 1.5 mm, and seven rows, separated by 2 mm. The first column contains only the slit with no flanking grooves. Light transmission through the slits in this column is used to normalise the transmission in the remaining columns. Variations in transmission through each of the elements in the "slits only" column provide a measure of the uniformity of the FIB fabrication process. Each entire matrix of structures is flanked

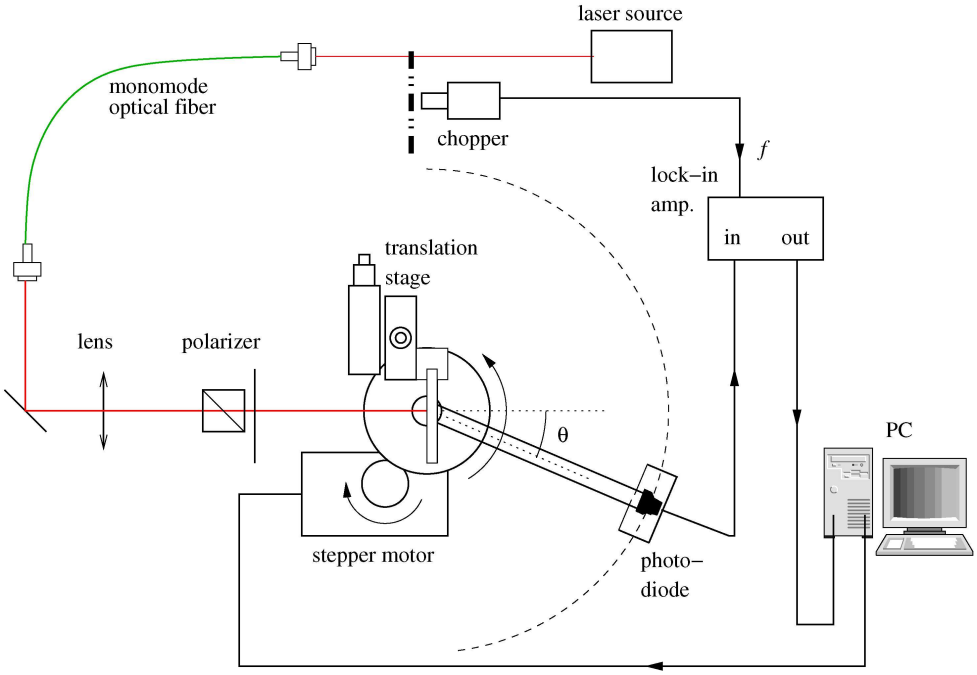

Figure 5. Goniometer setup for measuring far-field light intensity and angular distributions. A stabilised single mode CW diode laser, locked to a wavelength of 852 nm and modulated at 850 Hz by a chopper wheel, is injected into a single-mode fibre and focused onto the nanostructures mounted in a X-Y translation stage as shown. A stepper motor drives the goniometer arm, and the chopped light intensity detected by the photodiode is fed to a lock-in amplifier. Output from the lock-in is registered by the PC that also drives the stepper motor.

on one side by a small round hole and on the other by a line grating for absolute reference positioning and angular alignment of the structure matrix with respect to the input laser beam. The square microscope slides themselves, commercially available from SPI Supplies, are 25 mm on a side and 1 mm thick.

3.2. Goniometer setup

Measurements were carried out using a home-built goniometer shown in Fig. 5. Output from a diode laser source, temperature stabilised and frequency-locked to $^2S_{1/2}(F = 4) \rightarrow {}^2P_{3/2}(F = 4, 5)$ crossover feature in a Cs saturated absorption cell, is modulated at 850 Hz by a mechanical chopper, fed to a monomode optical fibre, focused and finally linearly polarised before impinging on the subwavelength structure mounted in the sample holder. The beam waist diameter and confocal parameter of the illuminating source are 300 μm and 33 cm, respectively. Throughout this series of measurements the laser power density was maintained $\sim 1\text{Wcm}^{-2}$. The sample holder itself is fixed to a precision x-y translator, and multiple structures, FIB-milled in a 2-D array on a single substrate, are successively positioned at the laser beam waist. A photodiode detector is mounted at the end of a 200 mm rigid arm that rotates about an axis passing through the centre of the sample holder. A stepper motor drives the arm at calibrated angular increments of 2.05 mrad per step, and the overall angular resolution of the goniometer is $\simeq 4$ mrad. The photodetector output current is fed to a lock-in amplifier referenced to the light chopper wheel. Data are collected on a personal computer that also controls the goniometer drive.

4. RESULTS

The CDEW model predicts three essential properties of the surface-wave response to light-source excitation: (1) a composite surface wave expressed by Eq. 5 and approximately represented by a damped harmonic wave, Eq. 4, with a wave vector $k = 2\pi n_s/\lambda_0$; n_s the surface index of refraction and λ_0 the wavelength of the source field, E_i, (2) a phase shift of $\pi/2$ in the damped cosine approximation to the CDEW with respect to the input plane wave at the slit midpoint and (3) a CDEW amplitude that decreases inversely with distance from the slit.

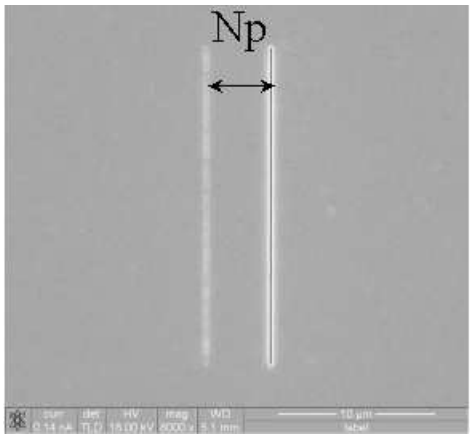

Figure 6. Scanning electron microscope (SEM) image of one of the series of single-slit, single-groove structures FIB milled into a 400 nm thick silver layer deposited on flat quartz microscope slides 1 mm thick. The width of both the slit and the groove is 100 nm, the height 20μm and the groove depth $\sim$ 100 nm. The distance Np is the pitch increment p = 104 nm multiplied by the number of increments N.

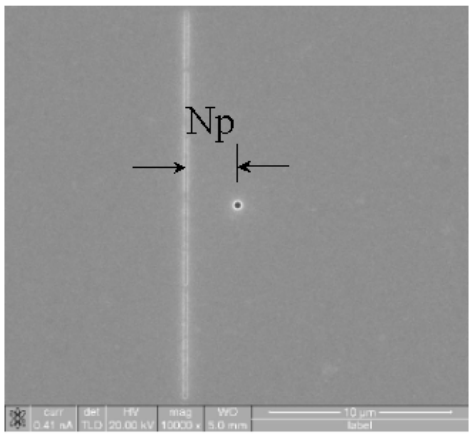

Figure 7. SEM image of one of the series of single-groove, single-hole structures fabricated in the same way as for single-groove, single-slit structures. The width of the groove is 400 nm, and the diameter of the hole is 400 nm. The distance Np is the pitch increment p = 50 nm multiplied by the number of increments N

We have carried out a series of measurements on simple 1-D structures to test these predictions. The structures consist of a single subwavelength slit or hole flanked by one subwavelength groove. We have carried out measurements with grooves of two different widths (100 nm and 415 nm) and depths varying from 32 nm to 256 nm. The grooves are FIB milled, and the distance between the slit and the grooves x_{sg} is systematically incremented in the fabrication process.

4.1. Structures with groove facing input side

Figures 6, 7 show one of the series of structures consisting of one slit and one groove and one hole and one groove, respectively. The separation between the slit and the grooves x_{sg} is indicated as Np where p is the basic unit of distance increment, the "pitch," and N is the number of increments. In Fig. 6 the pitch p was taken to be 104 nm, approximately one-eighth the wavelength of the surface wave and N was varied from 4 to 59. Structural details of these devices are described in the caption of Fig. 6. The slit (hole)-groove structures were mounted facing the input side and exposed to plane-wave radiation from the focused TEM_{00} laser source. Measurements of light intensity on the output side in the far field 200 mm from the plane of the structures were carried out using the goniometer setup described in section 3.2 and shown schematically in Fig. 5. The results are shown in Figs. 8, 9. The results show a damped oscillatory fringe pattern for both slit and hole structures, but the slit structures also exhibit a constant amplitude component that does not appreciably damp out to 6 μm slit-groove distance. As indicated in Fig. 3, and according to the CDEW model, the fringe pattern in the intensity of the output field E_o results from interference between the mode directly propagating through the slit at the input side E_t and a surface wave launched from the single-groove structures $E_{\rm cd}$. The model assumes that $E_{\rm cd}$ is reconverted to a propagating mode E_{sl} at the slit or hole; and it is this propagating mode that interferes with E_t. The frequency and phase of the interference pattern is a function of the slit (hole)-groove distance and any intrinsic phase shift with respect to E_t. The intensity I of the superposition term is given by

$$I = |E_t + E_{sl}|^2 = |\delta E_i + \beta\alpha E_i \exp i\gamma_i|^2 \tag{6}$$

The expression I for the intensity normalised to the intensity I_0 transmitted by a slit structure with no flanking grooves is

$$\frac{I(x_{sg})}{I_0} \propto 1 + \eta_i^2 + 2\eta_i \cos\gamma_i \quad \text{with} \quad \eta_i = \frac{\alpha\beta}{\delta} \tag{7}$$

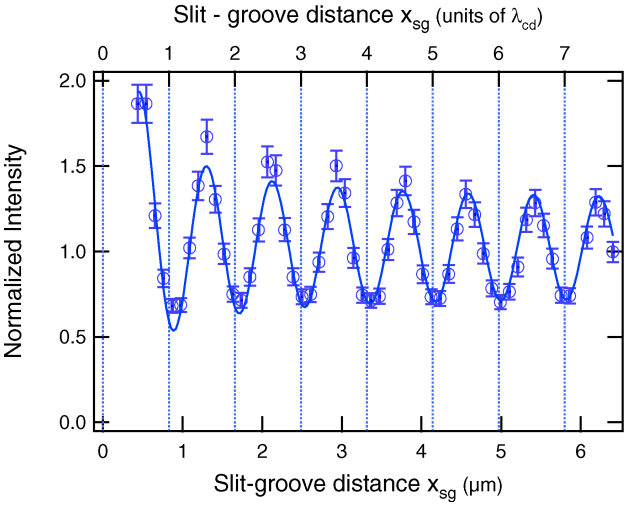

Figure 8. Normalised far-field intensity I/I_0 as a function of slit-groove distance x_{sg} for series of single-slit, narrow-groove structures mounted facing the input side with respect to plane wave excitation. Points are the measured data through which the solid line, a damped cosine wave with argument γ_i, (see Eqs. 8, 15) is fitted. The cosine wave amplitude damping is described by Eq. 15 with fitting parameters $\mu = 0.13 \pm 0.01$, $\kappa_{sl} = 0.12 \pm 0.01\,\mu$m and φ_i^s =?.

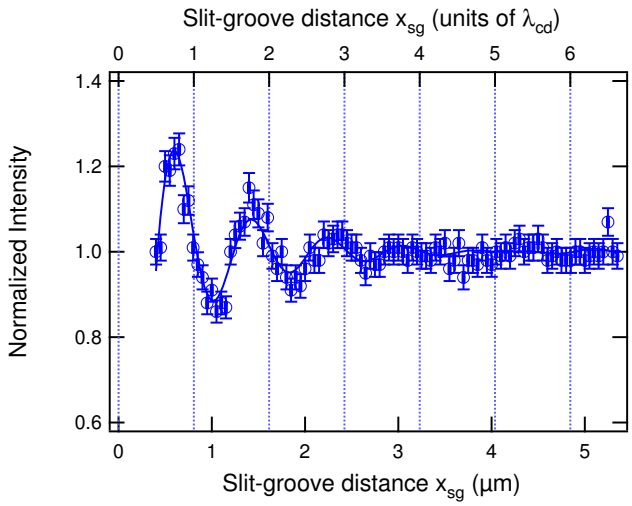

Figure 9. Normalised far-field intensity I/I_0 as a function of hole-groove distance x_{hg} for series of single-groove, small-hole structures mounted facing the input side with respect to plane-wave excitation. Points are measured data and the damped cosine wave was fit to the expression in Eq. 9b with parameter $\kappa_{hl} = 0.059 \pm 0.003\,\mu$m and $\varphi_i^h = 0.45 \pm 0.02\,\pi$.

In Eqs. 6, 7 $\alpha = E_{\rm cd}/E_i$ is the fractional amplitude of the surface wave launched from the incoming field E_i at the groove site x_{sg}, and β is the further fraction of this surface wave reconverted to a propagating wave at the slit, $E_{sl} = \beta E_{\rm cd} = \beta\alpha E_i$. The fractional amplitude of the directly transmitted component E_t is δ and the phase difference γ_i between E_t and E_{sl} is the sum of two terms,

$$\gamma_i = k_{\rm cd} x_{sg} + \varphi_i \tag{8}$$

The first term is the phase accumulated by the surface wave propagating from the groove to the slit and the second is any intrinsic phase shift resulting from the launch of the evanescent surface wave at the groove and its reconversion to a propagating wave at the slit. The term φ_i includes the nodal shift of the CDEW plus any phase shift associated with the detailed groove properties such as width and depth. Figures 8, 9 present a direct measure of the amplitude damping with distance, $\eta_i = \eta_i(x)$ and the period and phase of the oscillations, $\gamma_i = k_{\rm cd} x + \varphi_i$ from which the wavelength $\lambda_{\rm cd}$ of the surface wave, the phase φ_i, and the effective surface index of refraction n_s can be determined. Analysis of the frequency spectrum of the oscillations in Fig. 8, combined with a similar analysis of interference oscillations measured for output-side experiments (section 4.2) results in the determination of a surface wavelength $\lambda_{\rm cd} = 806 \pm 2.3$ nm and an effective surface index of refraction $n_s = 1.056 \pm 0.003$. The amplitude η_i of the oscillatory term depends on the slit-groove distance, and Figs. 8, 9 show that η_i falls of with increasing distance. For the interference pattern of Fig. 8 this fall-off is fit to an expression with two terms: an inverse distance dependence term plus a constant term. For the results of Fig. 9 the constant term is omitted.

$$\eta_i^{sl}(x_{sg})\cos(\gamma_i) = \left(\frac{\kappa_{sl}}{x_{sg}} + \mu\right)\cos(k_{\rm cd}x_{sg} + \varphi_i^s) \tag{9a}$$

$$\eta_i^{hl}(x_{hg})\cos(\gamma_i) = \left(\frac{\kappa_{hl}}{x_{hg}}\right)\cos(k_{\rm cd}x_{hg} + \varphi_i^h) \tag{9b}$$

with $\mu, \kappa_{sl,hl}$ the fitting constants as indicated in the captions of Figs. 8, 9 for slit and hole structures, respectively. The subscript i and superscripts sl, hl on η refer to input-side, slit and hole measurements, respectively. The

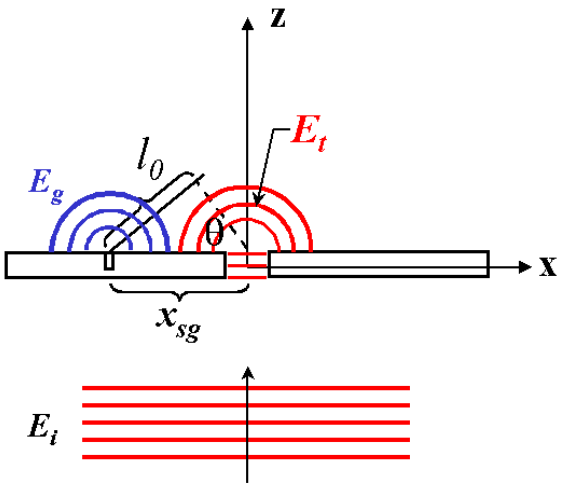

Figure 10. Diagramme showing the phase delay between E_t and E_g. The phase delay consists of three terms: the phase accumulation along the surface $k_{\rm cd}x_{sg}$, an angular component due to the optical path difference $l_0 = x_{sg}\sin\theta$, and any intrinsic phase delay φ_o between E_g and E_t.

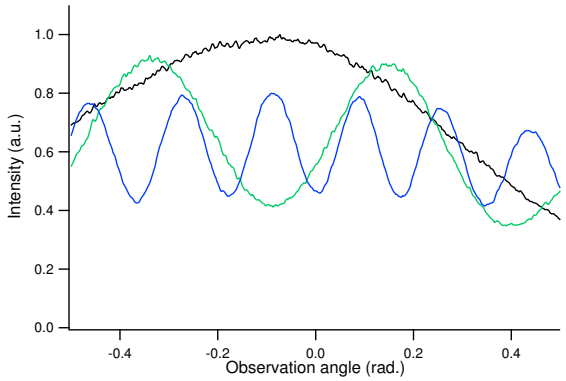

Figure 11. Selected output-side interference fringes for one-groove structures at three different slit-groove distances x_{sg}: black, 0.543 μm; green, 1.845 μm; blue, 4.991 μm.

subscript i and superscripts s, h on φ refer to input-side, slit and hole measurements, respectively.

4.2. Structures with groove facing output side

Measurements were also carried out with the subwavelength structures mounted facing the output side. As illustrated in Figs. 4 and 10, the far-field intensity pattern should exhibit interference between E_t directly propagating through the slit and E_g radiating from the grooves after having been transmitted by the surface waves $E_{\rm cd}$ launched at the output side of the slit. The frequency and phase of the interference pattern is a function of the slit-groove distance and any intrinsic phase shift of E_g with respect to E_t. Figure 11 shows interference patterns at selected slit-groove distances as a function of the goniometer detector angle θ (see Fig. 5) for narrow-groove structures. With a slit width of 100 nm and $\lambda_0 = 852$ nm, the fractional amplitude $\alpha = E_{\rm cd}/E_i$ launched on the output surface is, according to,[12] about 95%. The remaining 5% constitutes the amplitude fraction δ of the light directly transmitted through the slit E_t. Similar to the input-side case, a further fraction β is reconverted to propagating light E_g at the groove site x_{sg} and interferes with E_t. The intensity of the superposition emanating from structures flanked by one groove I_{1g} can be expressed as

$$I_{1g} = |E_t + E_g|^2 = |\delta E_i + \beta\alpha E_i \exp i\gamma_o|^2 \tag{10}$$

The normalised intensity I_{1g}/I_0 can then be expressed, with $\eta_o = \alpha\beta/\delta$,

$$\frac{I_{1g}}{I_0} \propto 1 + \eta_o^2 + 2\eta_o\cos\gamma_o \qquad \text{where} \quad \gamma_o = k_0 l_0 + \varphi \quad \text{with} \quad l_0 = x_{sg}\sin\theta \quad \text{and} \quad \varphi = k_{\rm cd}x_{sg} + \varphi_o \tag{11}$$

The relations between l_0, x_{sg}, θ are shown in Fig. 10. Similar to the input-side measurements, the frequency and phase of the interference pattern depend on the slit-groove distance through the term $k_{\rm cd}x_{sg}$, but in the output-side case there is an additional angular term in the optical path difference $k_0 x_{sg}\sin\theta$. Any intrinsic phase difference between E_t and E_g is represented by the term φ_o. With the goniometer detector rotated to a position directly perpendicular to the plane of the structure ($\theta = 0$) the expression for the normalised intensity, Eq. 11 simplifies to

$$\frac{I_{1g}}{I_0} \propto 1 + \eta_o^2 + 2\eta_o\cos(k_{\rm cd}x_{sg} + \varphi_o) \tag{12}$$

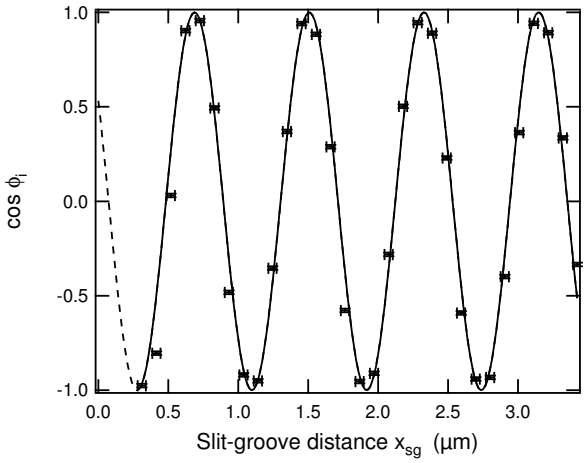

Figure 12. Narrow-groove structures: Plot of the phase $k_{\rm cd}x_{sg} + \varphi_o$ as a function of x_{sg} with the detector rotated to $\theta = 0$ on a line perpendicular to the structure plane. Extrapolation of the phase as x_{sg} approaches zero, yields $\varphi_0 = 0.32\,\pi \pm 0.02\,\pi$.

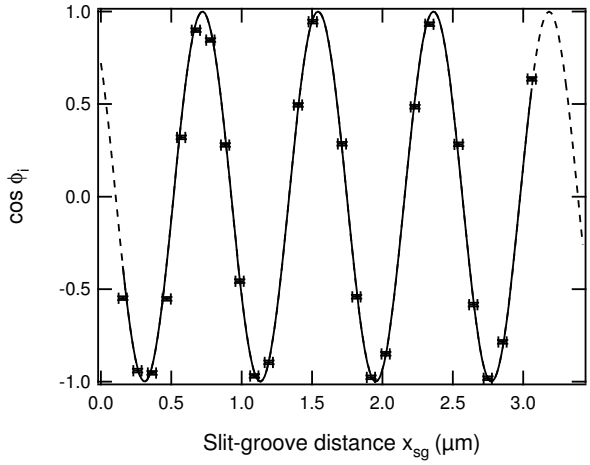

Figure 13. Wide-groove structures: Plot of the phase $k_{\rm cd}x_{sg} + \varphi_o$ as a function of x_{sg} with the detector rotated to $\theta = 0$ on a line perpendicular to the structure plane. Extrapolation of the phase as x_{sg} approaches zero, yields $\varphi_0 = 0.24\,\pi \pm 0.01\,\pi$.

Figures 12, 13 show plots of the cosine of the phase $k_{\rm cd}x_{sg} + \varphi_o$ as a function of x_{sg} for data sets from narrow-groove and wide-groove structures. With $k_{\rm cd} = 2\pi/\lambda_{\rm cd}$ known from the input-side measurements, the intrinsic phase φ_o is determined from the plot to be $\varphi_o = 0.32\,\pi \pm 0.02\,\pi$ and $\varphi_o = 0.24\,\pi \pm 0.01\,\pi$ for narrow- and wide-groove structures, respectively.

In addition to the frequency and phase of the interference we have studied the "visibility" or the contrast of the output-side interference fringes as function of x_{sg}. The interference contrast is defined as

$$C \equiv \frac{I_{max} - I_{min}}{I_{max} + I_{min}} \tag{13}$$

and according to Eq. 11 can be expressed as

$$C = \frac{2\eta_o}{1+\eta_o^2} \quad \text{or} \quad \eta_o = \frac{1-\sqrt{1-C^2}}{C} = \frac{\alpha\beta}{\delta} \tag{14}$$

Since $\alpha\beta = E_g/E_i$, the fractional amplitude radiating at a groove, a plot of η_o as a function of x_{sg} measures the dependence of this field amplitude on the slit-groove distance. Assuming that the conversion efficiency of $E_{\rm cd}$ to E_g at the groove is itself independent of the amplitude of the surface wave, the η_o dependence $\eta_o\,(x_{sg})$ on the slit-groove distance effectively measures the amplitude dependence of $E_{\rm cd}$.

$$\eta_o(x_{sg})\cos(\gamma_i) = \left(\frac{\kappa}{x_{sg}} + \mu\right)\cos(k_{\rm cd}x_{sg} + \varphi_o) \tag{15}$$

Figures 14, 15 show plots of η_o as a function of x_{sg} for narrow-groove and wide-groove structures, respectively. The form of the fitted curve through the data points, an inverse distance dependence with an additive constant, is give by Eq. 15 with fitting parameters μ, κ as indicated in the captions of Figs. 14, 15, respectively.

5. DISCUSSION

The measured interference fringes on both the input-side and output-side experiments confirm the presence of a surface wave of wavelength 806.8 ± 2.3 nm, determining a surface index of refraction $n_s = 1.056 \pm 003$. The CDEW model predicts a surface wave of the form expressed by Eq. 4 with a phase shift of $\pi/2$. The measured interferences show an intrinsic phase shift $\varphi_0 = 0.32\,\pi \pm 0.02\,\pi$ for the narrow-groove structures and

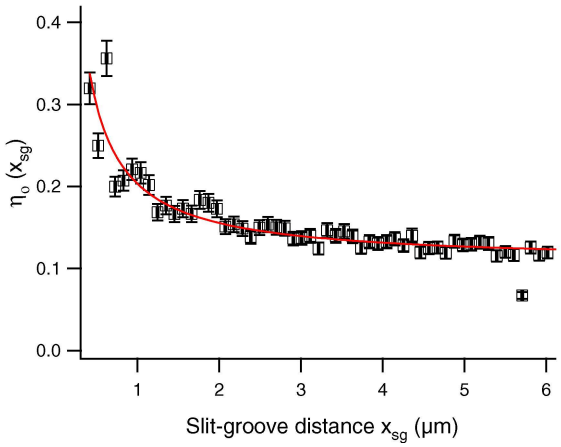

Figure 14. Narrow-groove structures: Plot of η_o as a function of the slit-groove distance x_{sg}. The quantity η_o is fit by Eq. 15 with fitting parameters $\mu = 0.13 \pm 0.01$ and $\kappa = 0.12 \pm 0.01 \mu$m.

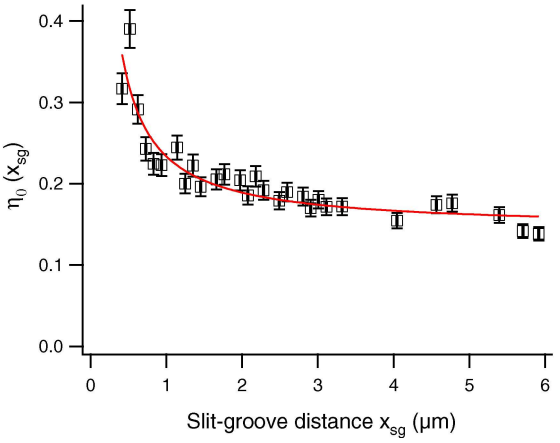

Figure 15. Wide-groove structures: Plot of η_o as a function of the slit-groove distance x_{sg}. The quantity η_o is fit by Eq. 15 with fitting parameters $\mu = 0.15 \pm 0.01$ and $\kappa = 0.11 \pm 0.01 \mu$m.

$\varphi_0 = 0.24\,\pi \pm 0.01\,\pi$ for the wide-groove structures, in disagreement with the expected CDEW phase shift of $0.5\,\pi$. However, as evidenced by the fact that the phase shifts differ between narrow- and wide- groove structures φ_0 must include not only a contribution from the intrinsic $\pi/2$ CDEW phase shift but also contributions arising from the form (width and depth) of the grooves themselves. The respective contributions of groove depth and width on the phase shift between the directly transmitted wave E_t and the reradiated wave E_g will be the subject of a subsequent report.

In addition to the intrinsic phase shift, measurements reveal an amplitude dependence consisting of two terms: one term exhibiting the inverse distance dependence predicted by CDEW and a second, constant term more consistent with a guided wave mode. We speculate that the constant component might be a manifestation of the surface plasmon-polariton, although the index of refraction predicted for this mode at a silver-air interface, $n_{sp} = 1.015$ is smaller than the measured index of refraction, $n_s = 1.056 \pm 0.003$ by about 10 standard deviations in the measurement uncertainty. This long-lived component can have a remarkably long survival length. We have carried out similar measurements to those reported here on structured silver films with slit-groove separations up to ($\sim 30\mu$m which continue to show an optical response from this presumably guided surface mode.

In summary these experiments have revealed that simple subwavelength structures produce surface waves with well-defined wavelength, amplitude and phase behavior with respect to the driving wave. The CDEW model can be used to rationalise elements of this behavior such as the net phase shift and the decreasing amplitude component, but at least in its present form does not explain the surprisingly efficient coupling to a guided surface mode.

5.1. References

REFERENCES

1. Ebbesen, T. W., Lezec, H. J., Ghaemi, H. F., Thio, T., and Wolff, H. J. Extraordinary optical transmission through sub-wavelength hole arrays. *Nature* **391**, 667-669 (1998).
2. Thio, T., Pellerin, K. M., Linke, R. A., Ebbesen, T. W., and Lezec, H. J. Enhanced light transmission through a single subwavelength aperture. *Opt. Lett.* **26**, 1972-1974 (2001).
3. Ghaemi, H. F., Thio, T., Grupp, D. E., Ebbesen, T. W., and Lezec, H. J. Surface plasmons enhance optical transmission through subwavelength holes. *Phys. Rev. B* **58**, 6779-6782 (1998).
4. Raether, H. *Surface Plasmons on Smooth and Rough Surfaces and on Gratings*, (Springer-Verlag, Berlin, 1988).
5. Barnes, W. L., Dereux, A., and Ebbesen, T. W. Surface plasmon subwavelength optics. *Nature* **424**, 824-830 (2003).
6. Treacy, M. J. Dynamical diffraction in mateallic optical gratings. *Appl. Phys. Lett.* **75**, 606-608 (1999).
7. Treacy, M. J. Dynamical diffraction explanation of the anomalous transmission of light through metallic gratings. *Phys. Rev. B* **66**, 195105-1–195105-11 (2002).
8. Cao, Q., and Lalanne, P. Negative role of surface plasmons in the transmission of metallic gratings with very narrow slits. *Phys. Rev. Lett.* **88**, 057403-1–057403-4 (2002).
9. García-Vidal, F. J., Lezec, H. J., Ebbesen, T. W.,and Martin-Moreno, L. Multiple paths to enhance optical transmission through a single subwavelength slit. *Phys. Rev. Lett.* **90**, 213901-1–213901-4 (2003).
10. Lezec, H. J. and Thio, T., Diffracted evansecent wave model for enhanced and suppressed optical transmission through subwavelength hole arrays. *Optics Express* **12**, 3629-3651 (2004).
11. Mandel, L. and Wolf, E. *Optical Coherence and Quantum Optics*, pp. 109-120 (Cambridge University Press, Cambridge England, 1995).
12. Kowarz, M. W. Homogeneous and evanescent contribution in scalar near-field diffraction. *Applied Optics* **34**, 3055-3063 (1995)
13. Born, M. and Wolf, E. *Prinicples of Optics*, 6th edition, pp. 370-401 (Pergamon Press, Oxford England, 1993).